Civil and Environmental Engineering
Vol. 0, Issue 0, DOI: 10.2478/cee-2026-0082

Experimental and Numerical Investigation of Flexural Behaviour in Steel Fiber-Reinforced Concrete Notched Beam

Danny Triputra SETIAMANAH[1], Priyo SUPROBO[1,*], Bambang PISCESA[1], Sinta Nabilah SALMA[2], Akbar Kalam RAMZY[1], Pannadipa Putera SUKMAJAYA[1], Wimpie Agoeng Noegroho ASPAR[3], Dwi Agus PURNOMO[3], Winda AGUSTIN[4], Shofwan LATHIF[4]

[1] Civil Engineering Department, Institut Teknologi Sepuluh Nopember, Kampus ITS Sukolilo, Surabaya 60111, Indonesia

[2] Department of Infrastructure Engineering, The University of Melbourne, Parkville 3010, Australia

[3] Research Center for Transportation Technology, National Research and Innovation Agency (BRIN), Jakarta 10340, Indonesia

[4] PT Wijaya Karya Beton Tbk (WIKA Beton), Jakarta 13340, Indonesia

* corresponding author: priyo@its.ac.id

Date of Submission:	21 November 2025
Revision Date:	16 December 2025
Date of Acceptance:	17 December 2025

Civil and Environmental Engineering
Journal of the Faculty of Civil Engineering | University of Žilina

Abstract

This study investigates the influence of hooked-end steel fibres on the compressive and flexural behaviour of steel fibre-reinforced concrete (SFRC) using combined experimental testing and three-dimensional nonlinear finite element analysis (3D-NLFEA). Concrete mixes with fibre volume fractions $V_f = 0\%$, 0.5%, 1.0%, and 1.5% were cast and tested through standard cylinder compression and notched-beam three-point bending. Notched beams were tested under three-point bending with crack mouth opening displacement (CMOD) control in accordance with JCI-S-002-2003, and the resulting load–CMOD responses were used to calibrate a 3D plasticity–fracture finite element model. Experimentally, the addition of steel fibres increased compressive strength from 52.52 MPa (plain concrete) to 70.55 MPa at $V_f = 1.5\%$, while the peak flexural load in notched beams rose from 36.01 kN to 49.24 kN with increasing V_f. SFRC mixes also exhibited markedly enhanced post-peak ductility and crack control, reflected in larger CMOD at comparable load levels and an extended descending branch of the load–CMOD curve. The calibrated 3D-NLFEA model reproduced the experimental load–displacement trends for all fiber contents with good agreement in peak load and overall curve shape, using post-cracking tensile contributions $f_{t,\mathrm{fib}}$ in the range of approximately 2.15–2.60 MPa. Within the limitations of the specimen set and modelling assumptions, the results suggest that moderate fibre contents (around 1.0–1.5%) provide a favourable balance between strength enhancement and flexural toughness and offer a rational basis for defining tensile softening laws in nonlinear analysis of SFRC elements. Further studies on reinforced members and structural-scale elements are recommended before translating these findings into codified design provisions.

Keywords

Notched beams; Finite element analysis; Load-displacement; Crack mouth opening displacement, Steel fibre reinforced concrete; 3D-NLFEA.

1. Introduction

Over the past several decades, concrete has been widely recognized as a reliable material for integrating steel reinforcement in the construction of infrastructure and building systems (Yoo & Yoon, 2015). Despite its high compressive strength, conventional concrete remains inherently vulnerable in tension, where localized microcracking can rapidly evolve into macrocracks, accelerating stiffness degradation and enabling the ingress of aggressive agents that compromise durability and long-term serviceability. To mitigate these limitations, fibre-reinforced concrete (FRC) has been developed as a multi-phase cementitious composite in which discrete fibres are dispersed throughout the matrix to provide crack-bridging capacity and enhanced post-cracking load transfer (Amer et al., 2021). Depending on performance requirements, fibres may be natural or synthetic (e.g., steel, glass, polypropylene, palm, or jute), and are selected to improve tensile response, crack control, ductility, and overall structural resilience (Flores-Nicolás et al., 2025; Kim et al., 2018; Tariq et al., 2023).Among these options, steel fibre-reinforced concrete (SFRC) is one of the most widely adopted forms of FRC due to the high stiffness and strength of steel fibres, their mechanical anchorage potential, and their effectiveness in controlling crack development under flexural and tensile actions.

When steel fibres are incorporated into concrete, they enable continued stress transfer across crack faces even after matrix cracking, thereby delaying localization and improving resistance to crack propagation and delamination (Deng et al., 2023).This post-cracking mechanism is commonly attributed to fibre bridging and pull-out, through which fibres dissipate energy in the fracture process zone and stabilize crack growth (Meda et al., 2012).While the inclusion of fibres typically produces modest changes in compressive strength and elastic modulus, it can substantially enhance residual tensile capacity and residual flexural performance, which are critical to maintaining integrity after first cracking and to achieving ductile failure modes (Iqbal et al., 2019a). Hooked-end steel fibres, provide improved mechanical anchorage and pull-out resistance, often producing a more stable post-peak response than straight or smooth fibres and supporting improved crack-width control under increasing deformation demand (Y. Zhang et al., 2020). From a structural design perspective, these residual properties are central to serviceability and ultimate limit state verifications, as they govern tensile stress redistribution and sectional capacity after cracking.

The inclusion of SF in concrete facilitates continuous stress transfer, even after the concrete matrix has begun to fail, thereby enhancing its resistance to cracking and delamination (Deng et al., 2023). Steel fibres operate through a bridging mechanism that absorbs strain energy in tension zones, helping to limit crack propagation and thus increasing the overall service life of the structure (Meda et al., 2012). Although the addition of SF has minimal impact on the compressive strength and elastic modulus of steel fibre-reinforced concrete (SFRC), it significantly improves its residual tensile and flexural strength (Iqbal et al., 2019). Hooked-end steel fibres offer superior pull-out resistance and exhibit more stable behaviour within the concrete matrix compared to other fibre types (Y. Zhang et al., 2020). In ultimate limit state (ULS) design, the residual flexural strength of SFRC is critical for determining the tensile stress distribution across the cross-section (Jin et al., 2025). Most design standards evaluate the residual tensile strength of SFC using the residual flexural tensile strength (F_t), typically obtained through beam testing.

Accordingly, contemporary assessment of SFRC increasingly emphasizes fracture-based descriptors in addition to conventional strength metrics. Key parameters include the crack mouth opening displacement (CMOD), stress–crack opening relationships, and fracture energy, each reflecting different aspects of post-cracking performance, toughness, and energy dissipation. Recent syntheses highlight that the fracture response of SFRC (e.g., load–CMOD behaviour, fracture toughness, and absorbed energy) is strongly controlled by fibre type, aspect ratio, and volume fraction, as well as by matrix characteristics and test configuration(Khalilpour et al., 2019; P. Zhang et al., 2023). Experimental and numerical studies further indicate that increasing steel fibre dosage generally improves tensile resistance after cracking, increases energy absorption, and enhances the stability of crack growth, resulting in improved ductility and reduced brittleness under flexure

(Dehghanpour et al., 2022; Rashidi et al., 2024). In design-oriented practice, residual tensile strength is often inferred from residual flexural tensile strength, F_t , derived from standardized beam testing, which provides a practical basis for characterizing post-cracking capacity for structural applications (Jin et al., 2025).

In parallel with advances in material characterization, there has been growing reliance on numerical simulation to interpret fracture processes and to generalize experimental findings beyond a single geometry or loading configuration. Recent contributions in *Civil and Environmental Engineering* illustrate this broader trend toward advanced composite action and computational assessment in concrete engineering. For example, near-surface mounted FRP strengthening systems have been shown to enhance flexural capacity and modify cracking behaviour in reinforced concrete members, underscoring the engineering value of fibre-based reinforcement solutions for extending service life and improving structural performance (Bdair & Alwash, 2025). Likewise, numerical studies on reinforced concrete members incorporating basalt FRP reinforcement further emphasize the role of finite element methods in evaluating cracking-related serviceability and capacity under durability-driven design scenarios (Almutairi et al., 2025). At the material scale, hybrid cementitious composites such as textile-reinforced engineered cementitious systems incorporating short polypropylene fibres have also been reported to improve flexural tensile response and interface-related performance, reinforcing the general principle that fiber additions can meaningfully enhance ductility and cracking resistance when appropriately designed (Hoang et al., 2025). Collectively, these studies motivate the continued integration of experimentally grounded fracture parameters into nonlinear simulation frameworks to better capture cracking, bridging, and post-peak response.

Against this background, the present study combines experimental three-point bending tests on notched SFRC beams with nonlinear finite element simulations using the 3D-NLFEA software suite. The numerical framework employs a three-dimensional nonlinear formulation to represent cracking and post-cracking behaviour, with SALOME used for preprocessing and *ParaView* for postprocessing. Previous investigations have demonstrated that 3D-NLFEA can accurately reproduce nonlinear responses of concrete elements under different confinement and reinforcement conditions and provide reliable agreement with measured structural behaviour (Piscesa et al., 2018, 2019, 2021). In this work, fracture-related parameters, including CMOD-based response and fracture energy, are explicitly incorporated to improve representation of steel-fibre bridging and crack evolution. The study therefore contributes (i) an experimentally supported evaluation of how steel fibre volume fraction modifies flexural response and fracture performance in notched beams and (ii) a calibrated 3D-NLFEA modelling approach capable of reproducing the observed load–displacement and load–CMOD behaviour with improved physical realism.

2. Experimental Investigation

2.1. Material Properties, Mix Design, and Specimen Geometry

Hooked-end steel fibres (DRAMIX 3D 65/35) were used as discrete reinforcement in this study. The fibres have a nominal length of 35 mm and a diameter of 0.55 mm (aspect ratio = 65), with a nominal tensile strength of approximately 1,345 MPa and a Young's modulus of about 210 GPa. Ordinary Portland Cement (OPC) Type I was used as the binder, and natural sand and coarse aggregate were employed as fine and coarse aggregates, respectively. Mixing water was potable tap water (pH ≈ 7). Workability was adjusted using a high-range water-reducing admixture (HRWR), Sika ViscoCrete-3115 N (polycarboxylate-based), selected to support high flowability and stable placement at low water–cement ratio. To enhance completeness and reproducibility, the principal physical properties of the constituent materials (e.g., cement specific gravity and fineness; aggregate gradation, specific gravity, and absorption; fibre geometry and mechanical properties; and admixture characteristics) are reported in a dedicated material-property (Table 1).

Four mixtures were prepared with a constant water–cement ratio of 0.28, while varying the steel fibre volume fraction (V_f) at 0%, 0.5%, 1.0%, and 1.5%. The corresponding mix proportions (cement, aggregates, water, and HRWR) and the equivalent steel fibre dosages (0, 11.9, 23.7, and 35.5 kg/m^3) are summarized in Table 1. The selected V_f range represents low, medium, and relatively high levels of fibre reinforcement that have been widely adopted in SFRC flexural applications to improve crack bridging, residual capacity, and energy absorption while maintaining workable fresh concrete (Lee et al., 2019; Salman et al., 2024.; Wang et al., 2023).

Table 1: Mix proportion of concrete specimens

Material	$V_f = 0\%$	$V_f = 0.5\%$	$V_f = 1.0\%$	$V_f = 1.5\%$
W/C	0.28	0.28	0.28	0.28
Cement (kg/m^3)	732.14	732.14	732.14	732.14
Aggregate (kg/m^3)	920.6	920.6	920.6	920.6
Sand (kg/m^3)	505.18	505.18	505.18	505.18
Water (kg/m^3)	207.05	207.05	207.05	207.05
Steel fibre (kg/m^3)	-	11.9	23.7	35.5
HRWR (kg/m^3)	7.32	7.32	7.32	7.32

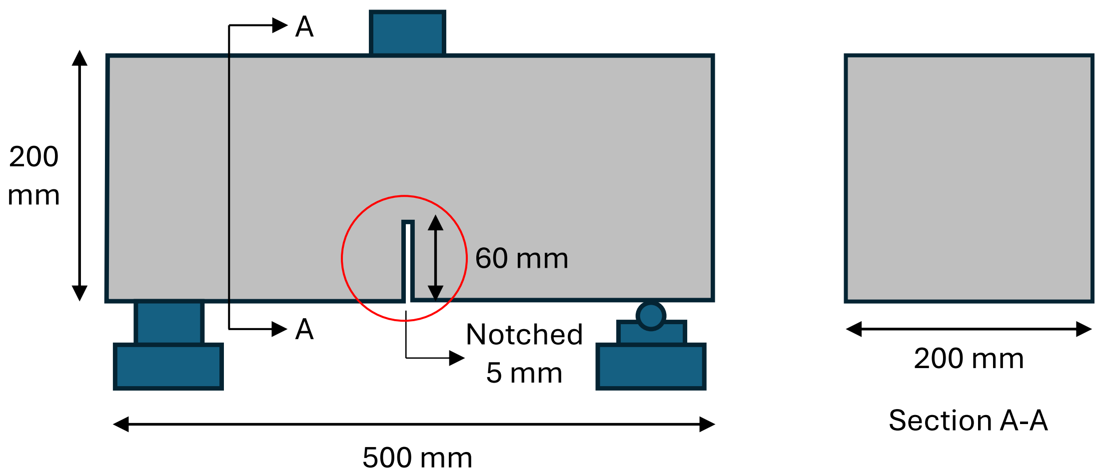

Figure 1: Notched beam specimen geometry

For compressive strength assessment, three cylinders (100 mm diameter × 200 mm height) were cast for each mixture (12 specimens total) and tested in accordance with ASTM C39/C39M. Flexural and fracture behaviour were evaluated using one notched beam per mixture (four beams total) tested under three-point bending following JCI-S-002-2003. The beam dimensions were 200 mm × 200 mm × 500 mm. A centrally located notch was provided with 5 mm width, 60 mm depth (≈0.30D), and 200 mm length, as shown in Figure 1.

2.2. Test Set-up and Procedure

After casting, the concrete specimens were demoulded after 24 hours and subjected to water curing for 28 days under controlled laboratory conditions. All specimens were carefully prepared for compressive strength tests and flexural tests that were conducted using Shimadzu 500 kN Universal Testing Machine (UTM). The set-up was equipped with a BDI data acquisition system with 16 high-speed channels, capable of recording up to 250 Hz. A TML linear variable transformer (LVDT) with a 100 mm displacement range was used to measure deformation, while loading was monitored using a TML load cell with a maximum capacity of 1 MN. To enhance the rigidity and stability of the testing system and ensure a more accurate representation of the stress-strain response, rigid columns were incorporated. The complete experimental setup for both compressive and flexural tests is shown in Figure 2.

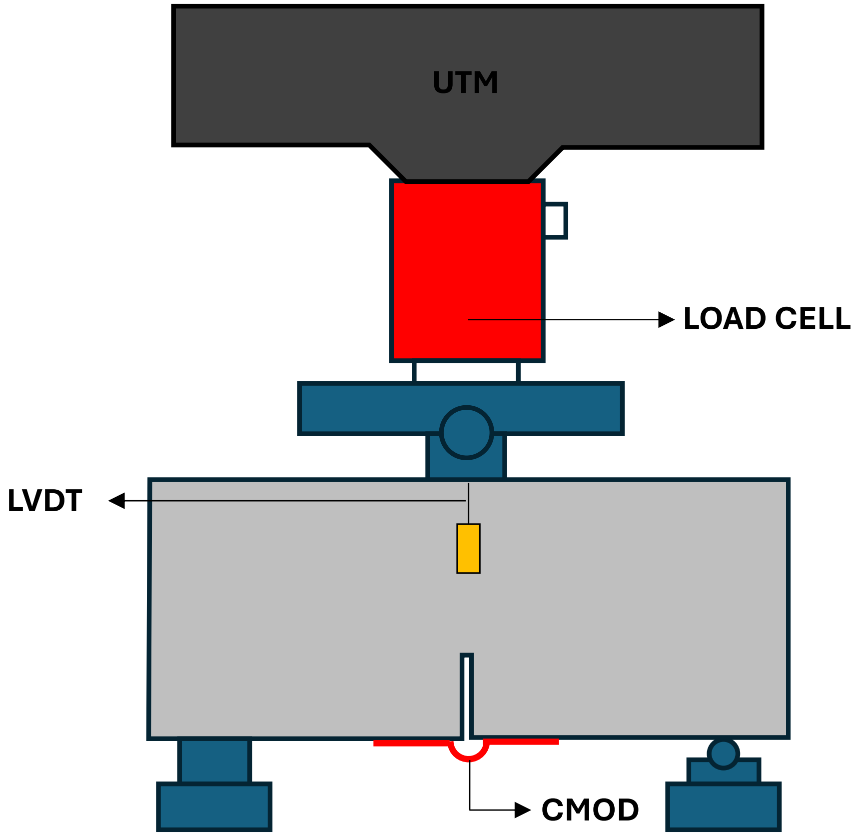

Figure 2: Test set-up: three-point flexural test

2.3. Finite Element Analysis

An in-house three-dimensional nonlinear finite element analysis (3D-NLFEA) program was employed to simulate the flexural study of steel fibre reinforced notched beams. Concrete behaviour is represented by a plasticity–fracture formulation originally developed for high-strength reinforced concrete columns (Piscesa et al., 2019b) and later extended to confined concrete (Piscesa et al., 2017). The model combines multi-surface plasticity with a fracture-energy criterion, enabling the capture of cover spalling, confinement effects and post-peak softening. Material parameters, particularly the frictional and hardening components, were calibrated against the stress–strain relationship for uniaxial and confined concrete proposed by (Samani & Attard, 2012). In this study, the mode-I fracture energy was taken as $G_{f0} = 0.03$ N/mm, consistent with the CEB–FIP Model Code 1990, and the reinforcing steel was described by a strain-hardening stress–strain law derived from experimental data so that the global response could be traced beyond peak load.

The geometry of the notched beam, shown in Figure 1, was constructed and meshed using the open-source pre-/post-processing platform SALOME version 9.11.0. An automatic tetrahedral mesh was adopted for its robustness and straightforward implementation. The resulting three-dimensional discretization is presented in Figure 3. The beam was modelled as simply supported: the left steel support was assigned pinned (hinge) boundary conditions, whereas the right support was defined as a roller, restraining vertical but not horizontal movement. The loading platen was left unrestrained in both horizontal and vertical directions so that it could follow the deformation of the beam. Loading was applied in displacement control at mid-span to determine the ultimate bending moment capacity and to examine the crack pattern at the peak load-carrying capacity of notched beam. Because cracking is expected to initiate and localize around the mid-span notch, the mesh in this region was refined, with a maximum element size of 10 mm, while a coarser mesh was used away from the notch to reduce computational cost. Post-processing and visualization of crack evolution, stress fields and deformation shapes were carried out using *ParaView*.

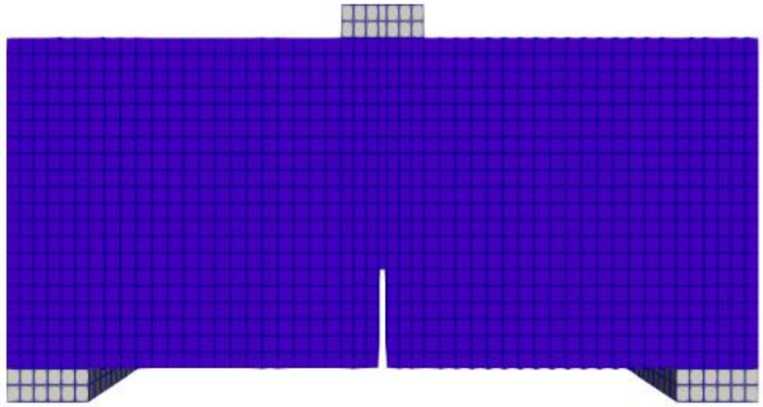

Figure 3: Meshed 3D model of notched beam (3DNLFEA)

3. Results and Discussion

3.1. Experimental Results

3.1.1. Concrete Compressive Strength

The compressive strength of the control mix (without steel fibres, $V_f = 0\%$) was measured at 52.52 MPa. The inclusion of steel fibers at volume fractions $V_f = 0.5\%$, 1.0%, and 1.5% increased the mean compressive strengths to 54.40 MPa, 58.72 MPa, and 70.55 MPa, respectively. Accordingly, steel fibres at 0.5%, 1.0%, and 1.5% increased the compressive strength by approximately 3.58%, 11.80%, and 34.33% compared with the control mix. This improvement is primarily attributed to the crack-bridging and confinement actions of the hooked-end fibres: under compression, the fibres intersect and bridge developing microcracks, transfer tensile stresses across the crack faces, and restrain lateral dilation of the concrete core. These mechanisms delay microcrack coalescence, increase the effective confinement of the matrix, and allow higher compressive stresses and strains to be sustained. A similar confinement-type contribution of steel fibres to axial strength and ductility has been demonstrated in constitutive modelling of SFRC under compression by (Puspitasari et al., 2020) , and in the finite-element analyses of notched SFRC beams by (Irmawan et al., 2022) in which fibre bridging and bond–slip friction were shown to enhance overall load-carrying capacity.

Figure 4(a) shows the corresponding axial stress–strain curves for all mixes. The initial slopes are comparable, indicating similar elastic stiffness; however, the SFRC mixes reach higher peak stresses and exhibit a more gradual post-peak softening than the control concrete. In particular, the mix with $V_f = 1.5\%$attains the highest peak stress and sustains significant stress at larger strains, demonstrating enhanced ductility and energy absorption. This response is consistent with experimental and meso-scale observations that steel fibers improve the integrity of the compressed concrete core and modify the post-peak behaviour through fiber-bridging stresses and residual bond across cracks (Zhao et al., 2023). The influence of fibre content on compressive strength is further illustrated in Figure 4(b), which plots the mean compressive strength f_c'versus $V_f$together with a linear regression fit. The relationship can be expressed as

$$f_c' = 2.1947V_f + 55.031 \quad (1)$$

Where:
f_c'- *in MPa,*
V_f- *in percent.*

Equation *(1)* indicates an approximately linear increase in compressive strength with fibre volume fraction within the tested range, with a noticeably steeper gain between $V_f = 1.0\%$and 1.5%. This steeper increment suggests that, beyond a certain fiber content, a denser three-dimensional fiber network is formed, which enhances internal confinement and improves stress transfer at the fiber–matrix interface. Comparable increases in compressive strength due to steel or hybrid fibres have been reported for lightweight, foamed, and pervious concretes (Abd Al Karem & Al-Asadi, 2024; Hemeda et al., 2024; Njyman & Hilal, 2025), and are consistent with recent meso-scale and micromechanical studies showing that steel-fibre bridging stresses enhance both static and dynamic compressive strength by inhibiting microcrack growth.

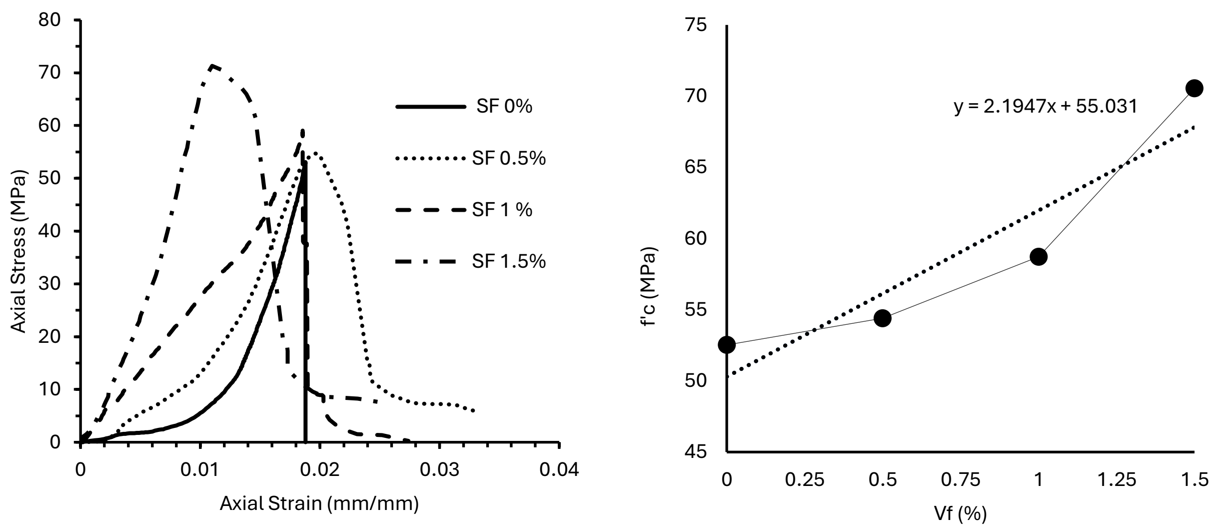

(a) (b)

Figure 4: (a) Compressive strength test results: stress-strain curve; (b) Relationship between peak load and volume fraction (V_f) of steel fibres

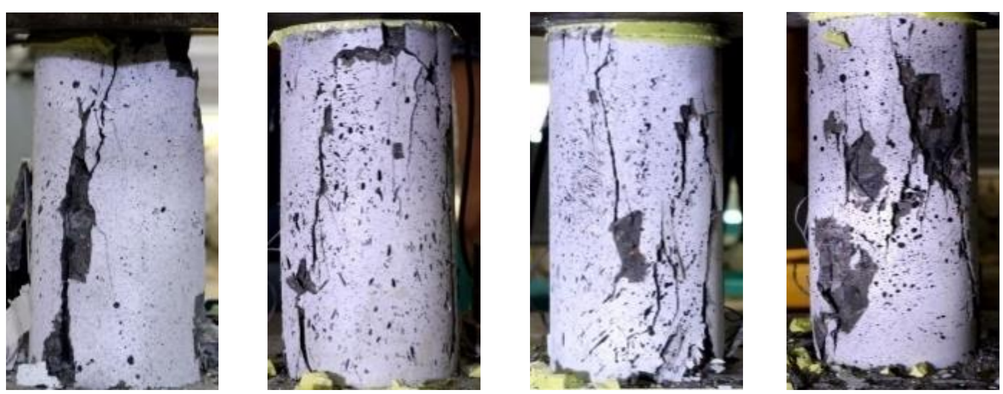

(a) V_f = 0% (b) V_f = 0.5% (c) V_f = 1.0% (d) V_f = 1.5%

Figure 5: Crack propagation patterns observed in uniaxial compression tests

The crack propagation patterns observed in cylindrical specimens subjected to uniaxial compression are illustrated in Figure 5. The control specimens, shown in Figure 5(a), exhibit major cracking concentrated along the loading axis, with the cementitious matrix providing the sole resistance. In contrast, the SFRC specimens in Figures 5(b)–5(d) display more restrained crack development and finer, more distributed cracking. Fiber-bridging across crack faces limits crack propagation and supports the concrete core after peak load, thereby enhancing post-peak performance. This observation is in line with the notion that the contribution of steel fibres becomes increasingly significant as the stress level approaches a high fraction of the ultimate compressive strength, at which point the tensile resistance of aggregates and the bridging action of fibres jointly inhibit crack widening and improve the post-peak behaviour of the concrete(Mishra et al., 2017).

3.1.2. Flexural Strength

Figure 6 shows the post-test crack propagation patterns observed in the notched beams subjected to three-point bending. The corresponding mechanical responses are presented in Figures 7 and 8. The control specimen ($V_f = 0\%$) reached a peak load of 36.01 kN. With the inclusion of hooked-end steel fibers, the peak load increased to 43.26 kN, 45.94 kN, and 47.65 kN for $V_f = 0.5\%$, 1.0%, and 1.5%, respectively, representing increases of 20.12%, 27.55%, and 32.31% relative to the control. This enhancement is attributed to fiber crack-bridging across the notched ligament after matrix cracking, which enables tensile stress transfer through the fiber–matrix bond and mechanical anchorage, delays crack localization, and increases the fracture resistance of the section.

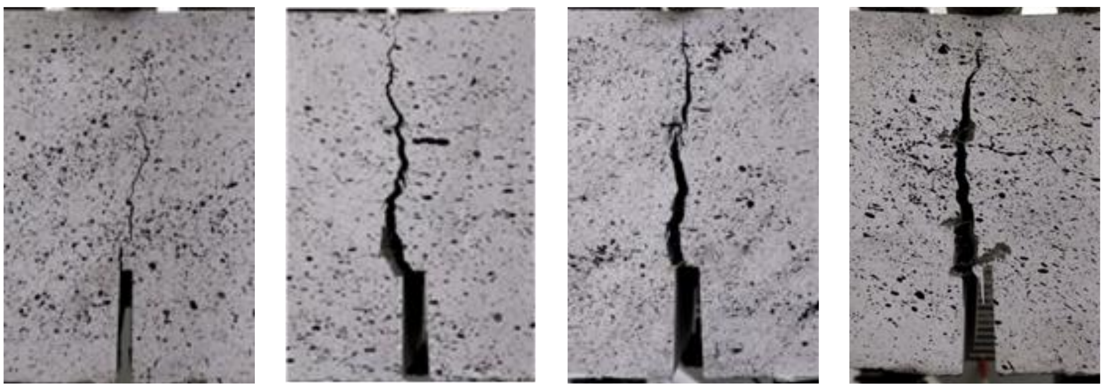

(a) V_f = 0% (b) V_f = 0.5% (c) V_f = 1% (d) V_f = 1.5%

Figure 6: Crack propagation patterns observed in notched beam

The crack patterns in Figure 6 are consistent with these trends. The plain concrete beam exhibits a dominant localized crack and limited resistance once cracking initiates, reflecting unstable fracture. In contrast, the SFRC beams show more controlled crack development and restrained crack opening, indicating that fibres contribute to stabilizing the fracture process zone and sustaining load transfer after cracking.

Figure 7 presents the load–displacement curves, which clearly distinguish the brittle response of the control specimen from the more ductile behaviour of SFRC. The control beam shows a rapid post-peak strength loss and limited displacement capacity. By comparison, all SFRC beams exhibit an extended post-peak region with higher residual load, confirming improved deformation capacity and toughness due to progressive fibre engagement. For $V_f = 1.0\%$, a short load drop occurs at a displacement of approximately 3 mm, which is interpreted as a discrete crack extension event and/or the development of additional microcracking within the fracture process zone. Despite this localized stiffness reduction, the specimen continues to sustain a considerable residual load because fibers remain active in bridging the crack and transferring tensile stresses across the ligament. The curve for $V_f = 1.5\%$appears rougher (more serrated) in the post-peak region than the other SFRC responses, which is consistent with intermittent fiber debonding and staged pull-out events of hooked-end fibers. Importantly, the overall descending branch remains gradual, indicating stable softening and increased energy absorption at the highest fiber dosage.

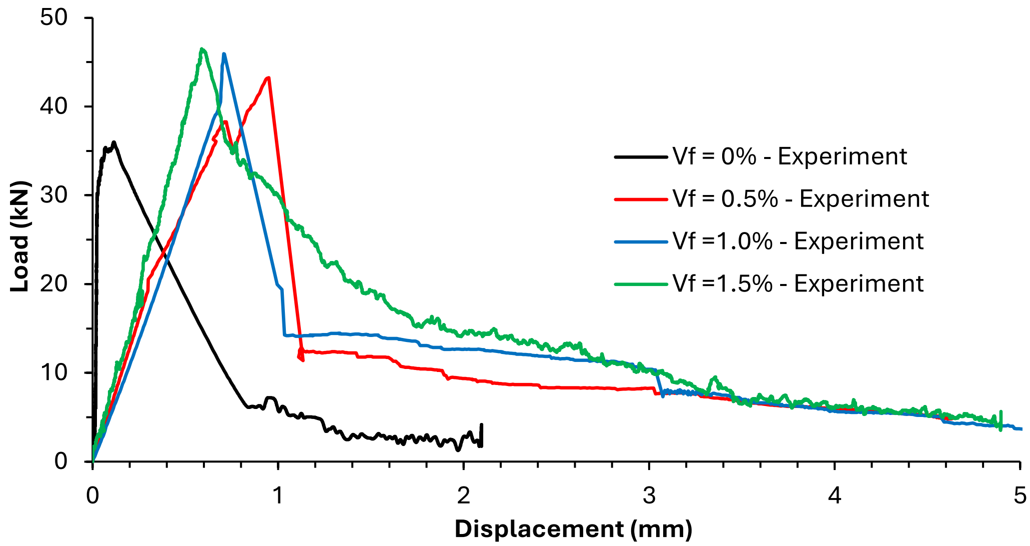

Figure 7: Load-displacement curve of notched beams

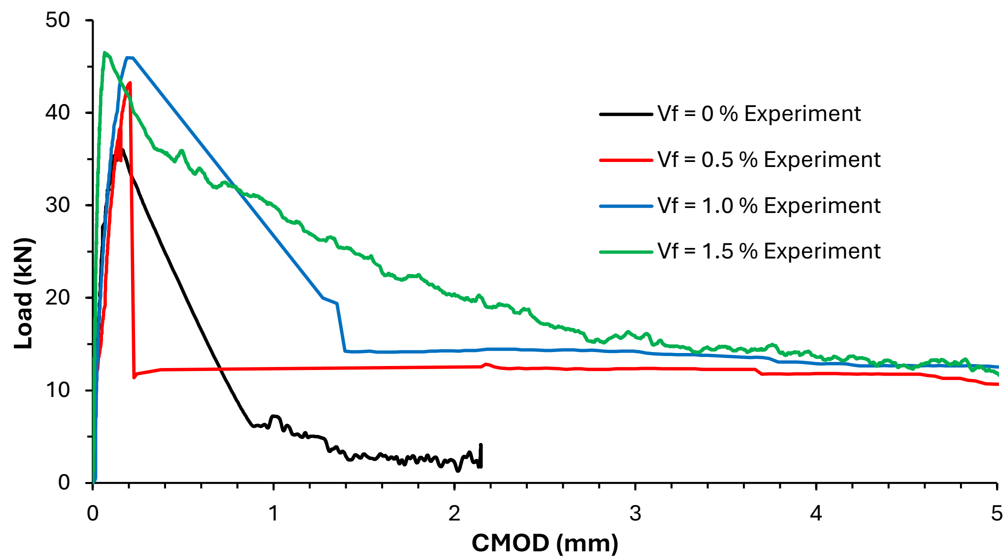

Figure 8: Load-CMOD curve of notched beams

Figure 8 shows the load–CMOD relationships during the pre-cracking and post-cracking phases. In all cases, the load increases as cracking initiates from the notch and reaches a maximum at peak load. Beyond the peak, the rate of load decay depends on fibre participation in the fracture process. As CMOD increases and the response enters the softening region, crack opening progresses while fibres progressively mobilize resistance through debonding and pull-out, thereby delaying crack widening. Consequently, specimens with $V_f = 1.0\%$and $V_f = 1.5\%$develop higher peak loads and maintain higher residual capacity over a wider CMOD range than the plain concrete and the $V_f = 0.5\%$mix. In contrast, the control beam exhibits a steep post-peak drop, indicating unstable crack propagation with negligible bridging once the matrix fractures. This dependency of fracture response on fiber content and bridging efficiency is consistent with fracture-based interpretations reported in the literature (J. Zhang & Stang, 1998).

Overall, increasing fibre volume fraction improves not only the peak load but also the post-peak response by enhancing crack-bridging capacity, delaying crack opening, and increasing energy absorption, in agreement with prior experimental findings on SFRC notched beams(Caggiano et al., 2012).

3.2. Numerical Analysis Results

3.2.1. Steel fibre tensile strength and crack opening displacement input

The tensile fracture input adopted in this study follows the SFRC tension-softening concept proposed by (Irmawan et al., 2022), in which the overall tensile response is constructed by superimposing two independent traction–separation laws: (i) the matrix softening and (ii) the steel-fibre bridging contribution. The matrix part is defined directly in terms of uniaxial tensile stress versus crack opening displacement, w, so that the fracture energy is dissipated through a crack-opening–based softening law rather than a strain-based law. For finite-element implementation, the crack opening is related to the strain field using an internal length scale, L_t, taken as the element characteristic size; this treatment reduces mesh sensitivity by ensuring that the prescribed softening is associated with crack opening instead of element-dependent strains.

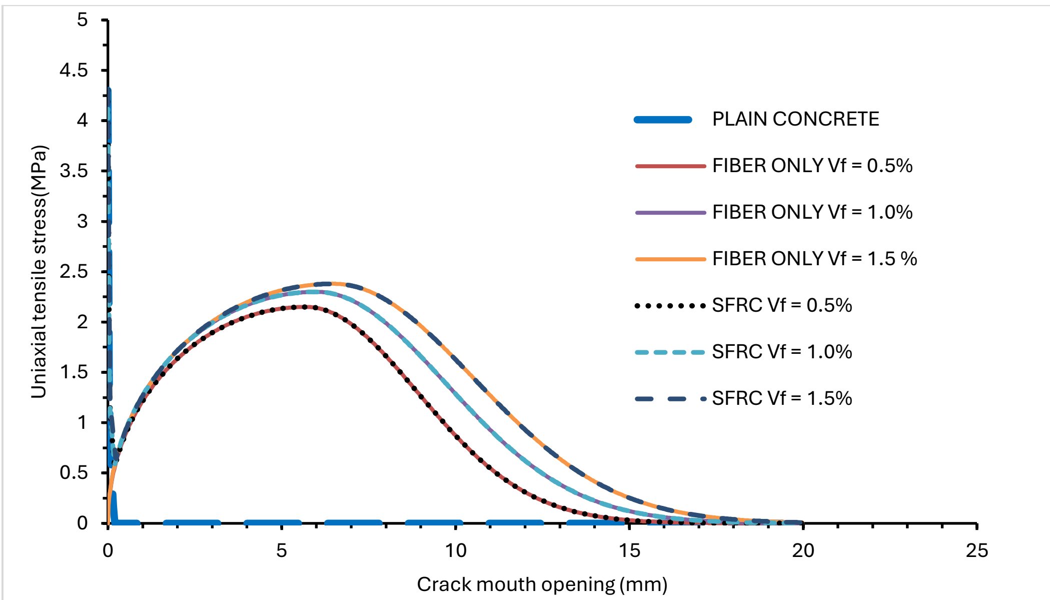

Figure 9: Uniaxial tensile contribution for steel fibre function of the crack mouth opening (CMO)

The fibre part is activated after cracking, and its bridging traction is formulated to capture the main mechanisms of (a) activation delay due to an initial slip, Δ, (b) gradual hardening up to a peak fiber tensile contribution at a characteristic crack opening, w_p, and (c) post-peak softening toward a residual tensile level that may persist due to bond–slip friction during pull-out. In the adopted formulation, the fiber-law shape is governed by hardening and softening functions, while the key parameters are anchored to the peak and residual fiber tensile contributions (e.g., $f_{t,\mathrm{fib}}$and $f_{r,\mathrm{fib}}$), which are calibrated for each fiber volume fraction. The fracture energy contributed by the fibers can then be estimated by integrating the fiber bridging traction over the crack opening domain, with practical limits applied when a residual plateau is present. In the present work, the matrix tensile strength and fracture energy were taken from Section 3.1.1, and the post-cracking tensile contribution of the fibers was calibrated for $V_f = 0.5\%$, 1.0%, and $1.5\%$to generate the tensile stress–crack opening and corresponding load–CMOD relationships (Figure 9), which were subsequently used as constitutive input in the 3D-NLFEA to represent the steel-fiber contribution in tension.

3.2.2. Load – displacement Result

All numerical models employed the same compressive strength as specified in Section 3.1.1 and a matrix fracture tensile strength of the plain concrete $f_t = 4.3\text{MPa}$. The additional post-cracking tensile contribution provided by the steel fibers, $f_{t,\mathrm{fib}}$, was varied with the fiber volume fraction V_f of each beam and calibrated such that the numerical load–displacement curves reproduce the experimental responses. This calibration is intended to ensure that the adopted post-cracking tensile transfer (governed by fiber bridging and pull-out) is represented consistently at the structural scale of the notched three-point bending test.

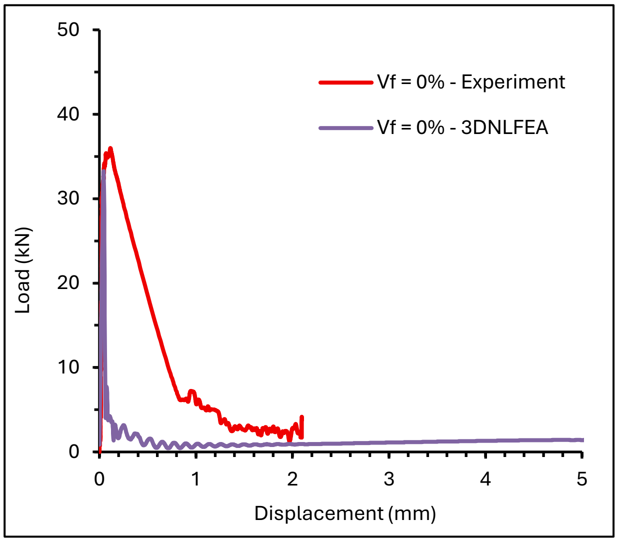

(a) $V_f = 0\%$

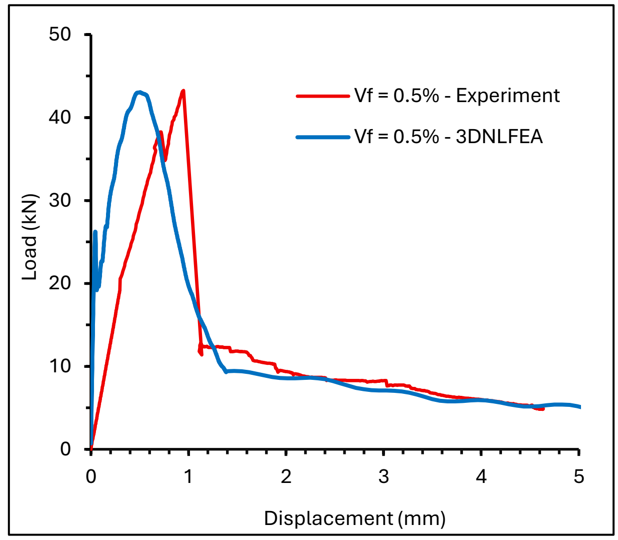

(b) $V_f = 0.5\%$

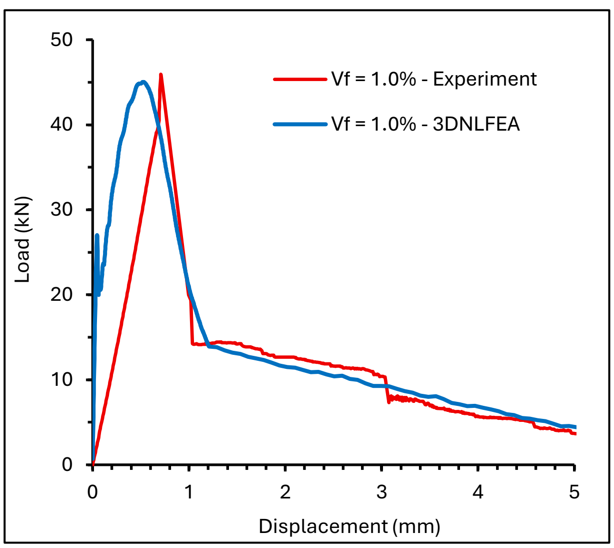

(c) $V_f = 1.0\%$

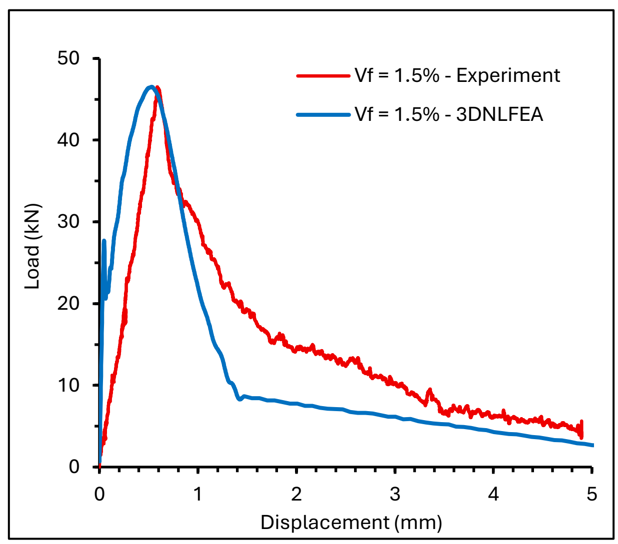

(d) $V_f = 1.5\%$

Figure 9: Load-displacement curves result for notched beams with varying fibre volume fractions

Figure 10(a) compares the experimental and numerical results for the notched beam without fibres ($V_f = 0\%$). As no steel fibers were present, no $f_{t,\text{fib}}$ value was assigned, and the numerical model predicted a peak load of 30.16 kN. The differences between the two curves are primarily associated with the post-peak regime, where the response becomes highly sensitive to crack localization and fracture energy assumptions. In the experiment, the descending branch reflects the development of a fracture process zone and progressive crack opening, while the numerical response exhibits a more idealized and sharper loss of load-carrying capacity once the crack localizes in the model.

For the beam with $V_f = 0.5\%$, shown in Figure 10(b), $f_{t,\text{fib}}$ was set to 2.15 MPa and the numerical peak load was 43.47 kN. The numerical curve provides a close representation of the experimental trend up to the maximum load, including the initial stiffness and the peak level. After the peak, both curves enter the softening regime, where the applied load decreases while the displacement continues to increase due to ongoing crack opening and progressive fiber debonding/pull-out. In this region, the numerical curve shows a slightly steeper reduction and generally lower residual load than the experiment. This discrepancy is attributed to the fact that the numerical model represents fibre action through an averaged constitutive assumption, whereas the experimental specimen is influenced by spatial variability in fibre distribution/orientation and bond conditions, which can promote a more gradual and energy-dissipative post-peak response. In addition, the measured displacement may include contributions from local seating/indentation at supports and loading points and from test-system compliance, which are not explicitly represented in the idealized boundary conditions of the simulation (Kaklauskas et al., 2024).

Figure 10(c) presents the results for the beam with $V_f = 1.0\%$, where $f_{t,\mathrm{fib}} = 2.30$MPa and the numerical peak load reached 46.58 kN. Again, the agreement is strong up to the peak load, while differences become more visible beyond peak. The experimental curve exhibits localized drops/changes in slope that are typical of unstable crack advance and discrete pull-out events as the crack propagates through a heterogeneous fiber field. By contrast, the numerical response is smoother because the crack evolution is represented in an averaged manner at the continuum level, which naturally suppresses abrupt load drops associated with localized micro-mechanisms (Mi et al., 2023).

Similarly, Figure 10(d) corresponds to $V_f = 1.5\%$with $f_{t,\mathrm{fib}} = 2.45$MPa, giving a numerical peak load of 49.24 kN. The model captures the increase in peak load with fiber dosage; however, the experimental post-peak branch remains higher and more gradual than the numerical prediction, indicating greater residual capacity and toughness in the test. This outcome is consistent with the physical role of higher fiber content in sustaining tensile transfer across the crack plane through progressive pull-out over an extended crack-opening range, while an averaged constitutive representation may underestimate residual bridging efficiency for specimens that develop favourable fibre alignment and engagement along the dominant crack path (Marcalikova & Cajka, 2020).

Overall, the simulations reproduce the key experimental trends: increasing V_f(and the calibrated $f_{t,\mathrm{fib}}$) enhances the peak load and improves the post-cracking load-carrying capacity of the notched beams due to fiber bridging. The remaining discrepancies are concentrated in the softening regime and are explained by the combined effects of (i) heterogeneity in fiber distribution/orientation and bond conditions, (ii) discrete cracking and pull-out events in experiments versus a smoother continuum representation in the numerical model, and (iii) test-system compliance embedded in measured displacements. These same considerations also explain why displacement-related measures can differ in stress–strain representations: experimental “strain” derived from global displacement over a finite gauge length is influenced by compliance and localization after cracking, whereas numerical strain is obtained from element-level (or averaged field) outputs under idealized boundary conditions, so identical stress levels do not necessarily correspond to identical strain/displacement once cracking localizes.

3.2.3. Crack Pattern

Figure 11(a) - (d) present the contours of the fracturing parameter for the notched beam obtained from the 3D-NLFEA simulations, with the plots focused on the mid-span region. In all cases, the fracture process initiates at the notch tip and propagates vertically towards the loading platen, forming a narrow crack band whose width is comparable to the notch width. This behaviour is consistent with previous numerical studies on steel-fibre-reinforced notched beams under three-point bending, where the fracturing parameter contours also showed a dominant crack band extending from the notch towards the compression zone beneath the loading platen (Irmawan et al., 2022). As the steel-fibre (SF) volume fraction increases from 0% to 1.5%, the simulated fracturing zone becomes more diffuse near the top surface, indicating enhanced crack-bridging and energy dissipation provided by the fibres.

The influence of the fibres on the global response is reflected in the peak load and mid-span displacement associated with each contour. For the plain concrete beam without fibres (SF = 0%), the peak load is 30.16 kN at a mid-span displacement of 0.44 mm. Adding 0.5% fibres increases the peak load to 43.47 kN with a corresponding displacement of 0.94 mm, while SF = 1.0% yields a peak load of 46.58 kN at 1.08 mm. The highest fibre content considered (SF = 1.5%) further raises the peak load to 49.24 kN, with the displacement at peak reaching 1.20 mm. This systematic increase in both load-carrying capacity and deformation at peak is in line with the observations of (Irmawan et al., 2022), who reported that steel fibres delay crack localizations, widen the region with elevated fracturing parameter beneath the loading platen, and lead to larger deflections at failure. Overall, the present fracture-parameter contours confirm that increasing the fibre content enhances the toughness of the notched beam and promotes a more distributed damage pattern rather than a single brittle crack.

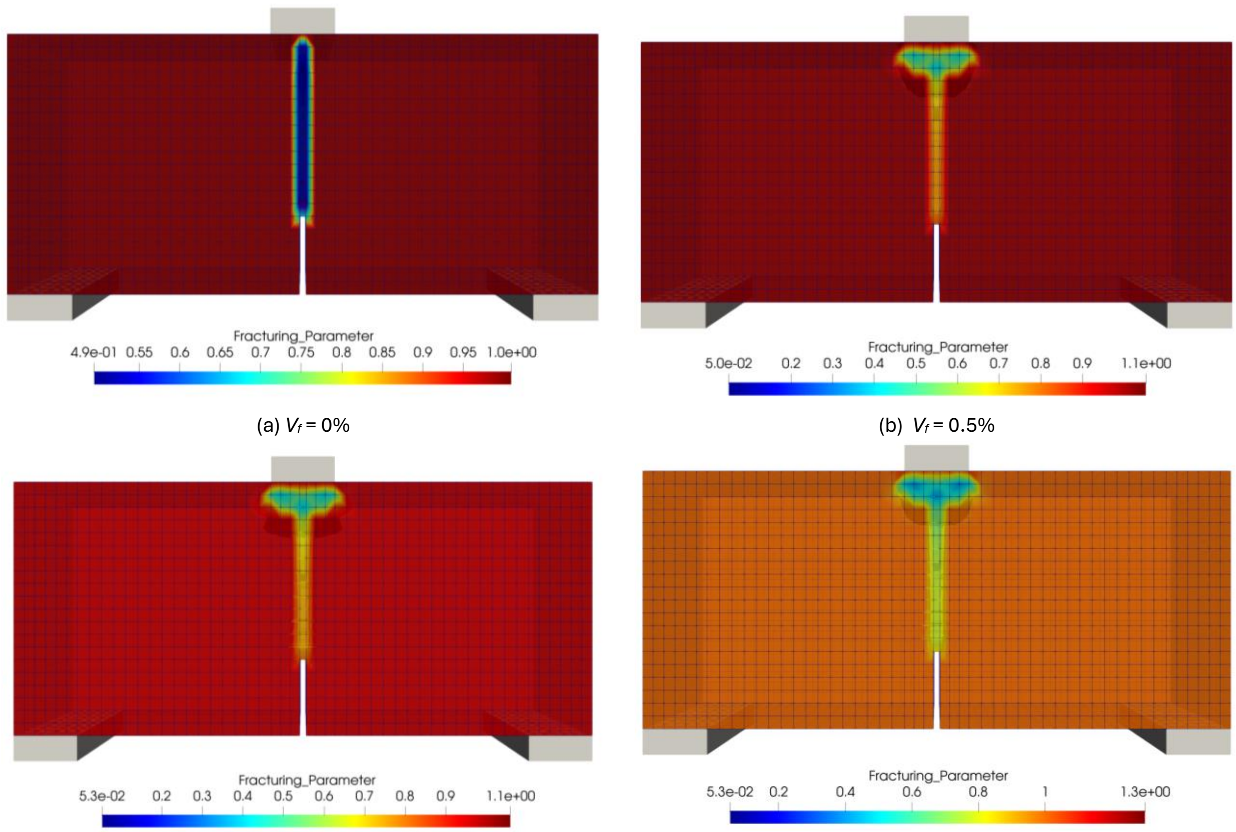

(a) V_f = 0% (b) V_f = 0.5%

(c) V_f = 1% (d) V_f = 1.5%

Figure 10: Fracturing parameter contour plots for notched beam

Figure 12(a)–(d) show the crack mouth opening displacement (CMOD) contours obtained from the 3D-NLFEA simulations of the notched beam for fibre volume fractions V_f = 0, 0.5, 1.0, and 1.5%. CMOD is evaluated at the notch mouth at mid-span, in accordance with three-point bending procedures for notched beams in which the load–CMOD response is recorded to characterize fracture energy and residual flexural performance of fibre-reinforced concrete (Paegle et al., 2016; Rismayanti et al., 2025). In all four cases, the crack initiates at the notch tip and propagates upward, with the largest CMOD values concentrated along the notch lips and within the vertical crack band. As the steel-fibre content increases, the region with significant crack opening becomes more extended and more diffuse near the compression zone, indicating a more gradual localization of damage and stronger crack-bridging action by the fibres (Irmawan et al., 2022)

The numerical results at peak load are summarized in Table 2. For the plain concrete beam (SF = 0%), the peak load is 30.16 kN at a mid-span displacement of 0.44 mm, with a CMOD of 0.008 mm. Introducing 0.5% steel fibres increases the peak load to 43.47 kN, accompanied by a mid-span displacement of 0.93 mm and a CMOD of 0.61 mm. For $V_f = 1.0\%$, the beam reaches 46.58 kN at 1.08 mm mid-span displacement with a CMOD of 0.62 mm, whereas the highest fibre content considered ($V_f = 1.5\%$) attains 49.24 kN with 1.18 mm displacement and a CMOD of 0.682 mm. Thus, higher fibre volume fractions allow the beam to sustain both larger crack openings and greater deflections at higher load levels. This trend is consistent with recent experimental and numerical studies on SFRC notched beams, which show that steel fibres bridge the crack, transfer tensile stresses across the crack faces and enlarge the area under the load–CMOD curve, thereby increasing fracture energy and overall toughness. Overall, the present CMOD results confirm that steel fibres markedly enhance the resistance of the notched beam to crack opening prior to failure.

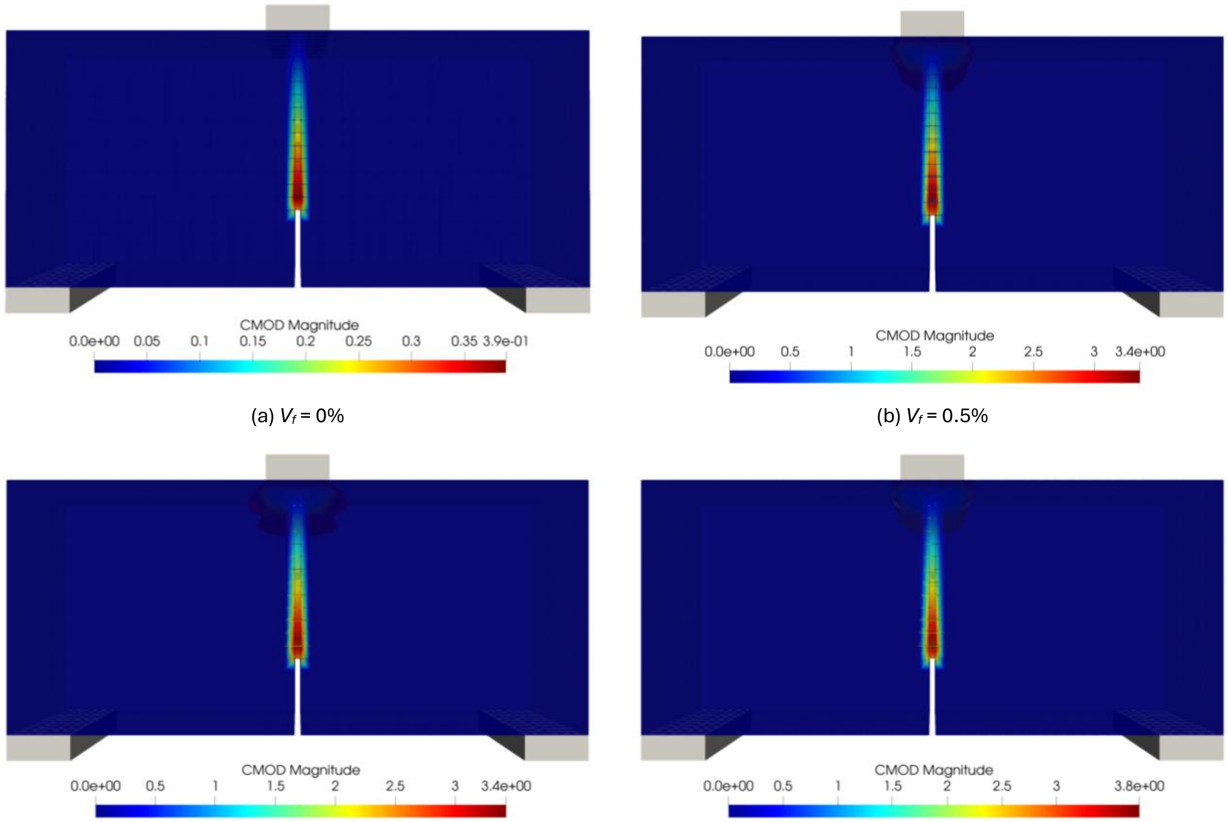

(a) $V_f = 0\%$ (b) $V_f = 0.5\%$ (c) $V_f = 1\%$ (d) $V_f = 1.5\%$

Figure 11: Crack mouth opening displacement (CMOD) contour plots for notched beam

Table 2: Displacement and CMOD at peak load for different fibre volume fractions.

V_f (%)	Peak load (kN)	Mid-span displacement (mm)	CMOD (mm)
0	30.16	0.44	0.008
0.5	43.47	0.93	0.61
1	46.58	1.08	0.62
1.5	49.24	1.18	0.682

4. Conclusion

This study investigated the influence of hooked-end steel fibres (DRAMIX 3D 65/35) on the compressive and flexural performance of concrete through cylinder compression tests, notched-beam three-point bending tests, and complementary 3D nonlinear finite element analyses (3D-NLFEA). Under compression, incorporating steel fibres increased the mean strength from 52.52 MPa (control) to 70.55 MPa at $V_f = 1.5\%$. In flexure, the notched-beam response showed a consistent increase in peak load from 36.01 kN to 49.24 kN with increasing V_f, accompanied by markedly enhanced post-peak ductility and crack-width control (CMOD increasing from approximately 0.008 mm to approximately 0.682 mm). These outcomes confirm that steel fibers effectively bridge cracks, promote stable post-cracking load transfer, and improve energy absorption relative to plain concrete.

The 3D-NLFEA simulations reproduced the experimental load–displacement trends across all fibre contents when the fibre-related post-cracking tensile contribution was represented using calibrated values of $f_{t,\mathrm{fib}}$of approximately 2.15–2.60 MPa. The minor overprediction of post-peak displacement is plausibly associated with specimen-level variability, particularly non-uniform fibre dispersion and orientation—rather than a fundamental limitation of the modelling approach. Within the scope of the investigated mixes, specimen geometry, and modelling assumptions, $V_f = 1.0\% - 1.5\%$appears to provide a balanced compromise between compressive strength enhancement and flexural toughness; where crack control and post-peak load-carrying capacity dominate, $V_f = 1.5\%$ produced the most pronounced improvements.

To strengthen the translation of these findings toward structural-scale practice and design guidance, future research will extend the present work in four targeted directions. First, the experimental matrix will be broadened by expanding the range of FRC mix designs and fibre dosages (including intermediate V_f levels) to better quantify dosage–performance relationships and identify practical thresholds. Second, the investigation will be scaled to structural members by testing reinforced beams and slab elements (full-scale or near full-scale) under monotonic and repeated loading, with emphasis on both serviceability metrics (crack-width evolution, stiffness degradation, residual deflection) and ultimate limit-state behavior. Third, the 3D-NLFEA framework will be advanced into a validated parametric tool by refining tensile softening laws using an expanded residual-strength database and by explicitly accounting for the effects of fibre orientation and dispersion on post-peak response. Fourth, and critically from a resilience and sustainability perspective, subsequent phases will evaluate more sustainable SFRC formulations by incorporating recycled constituents, particularly recycled steel fibres (and, where appropriate, other recycled materials), while assessing the coupled impacts on mechanical performance, crack control, durability-related behaviour, and constructability. Collectively, these steps provide a clear research roadmap for developing resilient, lower-impact SFRC systems and for supporting future design-oriented and code-consistent recommendations.

Acknowledgements

The authors gratefully acknowledge the financial support of Lembaga Pengelola Dana Pendidikan (LPDP) through the Riset dan Inovasi Program untuk Indonesia Maju (RIIM), under contract numbers 22/IV/KS/06/2022 and 2127/PKS/ITS/2022, for the research project “Redefining a New Resilient Slab-Track Structure for a High-Speed Train.” The authors also wish to thank PT Wijaya Karya Beton for their valuable technical assistance, including the provision of concrete materials and access to batching plant facilities.

Author Contributions

D.T.S collecting all data and managing the experimental and numerical analysis. **P.S.** overviewing and solving problems. **B.P.** supervised and designed the study. **S.N.S.** contributed to manuscript writing. **A.K.R.** conducted the experiments. **P.P.S.** performed the data analysis. All authors critically reviewed and approved the final version of the manuscript and agreed to be accountable for all aspects of the work. **W.A.N.A.** and **D.A.P.** (BRIN) were responsible for the design, preparation, and calibration of the test setup and supported specimen instrumentation. **W.A.** and **S.L.** (PT Wijaya Karya Beton) supported the experimental program by coordinating material supply, specimen casting, and testing logistics. All authors critically reviewed and approved the final version of the manuscript and agreed to be accountable for all aspects of the work.

Disclosure of Interest

The authors declare that they have no known competing financial interests or personal relationships that could have appeared to influence the work reported in this paper.

Data Availability Statement

The data supporting the findings of this study are available from the corresponding author upon reasonable request.

References

Abd Al Karem, S. T., & Al-Asadi, A. K. (2024). IMPACT OF VARIOUS TYPES OF FIBRES ON THE MECHANICAL PROPERTIES OF LIGHTWEIGHT CONCRETE. Civil and Environmental Engineering, 20(2), 1255–1266. https://doi.org/10.2478/cee-2024-0091.

Almutairi, A. L., Ahmed, S. N., & Domat, W. B. (2025). Numerical Analysis of Reinforced Concrete Members with Basalt Fibre Reinforced Polymer (BFRP) Bars. Civil and Environmental Engineering. https://doi.org/10.2478/cee-2025-0070.

Amer, A. A. R., Abdullah, M. M. A. B., Liew, Y. M., Aziz, I. H. A., Wysłocki, J. J., Tahir, M. F. M., Sochacki, W., Garus, S., Gondro, J., & Amer, H. A. R. (2021). Optimizing of the cementitious composite matrix by addition of steel wool fibers (chopped) based on physical and mechanical analysis. Materials, 14(5), 1–14. https://doi.org/10.3390/ma14051094.

Bdair, N. S. H., & Alwash, N. A. H. (2025). Flexural Strengthening of Reinforced Concrete Beams by Different FRP Products Using Near-Surface Mounted Technique. Civil and Environmental Engineering. https://doi.org/10.2478/cee-2025-0087

Caggiano, A., Cremona, M., Faella, C., Lima, C., & Martinelli, E. (2012). Fracture behavior of concrete beams reinforced with mixed long/short steel fibers. Construction and Building Materials, 37, 832–840. https://doi.org/10.1016/j.conbuildmat.2012.07.060.

Dehghanpour, H., Subasi, S., Guntepe, S., Emiroglu, M., & Marasli, M. (2022). Investigation of fracture mechanics, physical and dynamic properties of UHPCs containing PVA, glass and steel fibers. Construction and Building Materials, 328. https://doi.org/10.1016/j.conbuildmat.2022.127079.

Deng, Y., Zhang, Z., Shi, C., Wu, Z., & Zhang, C. (2023a). Steel Fiber–Matrix Interfacial Bond in Ultra-High Performance Concrete: A Review. In Engineering (Vol. 22, pp. 215–232). Elsevier Ltd. https://doi.org/10.1016/j.eng.2021.11.019.

Deng, Y., Zhang, Z., Shi, C., Wu, Z., & Zhang, C. (2023b). Steel Fiber–Matrix Interfacial Bond in Ultra-High Performance Concrete: A Review. In Engineering (Vol. 22, pp. 215–232). Elsevier Ltd. https://doi.org/10.1016/j.eng.2021.11.019.

Flores-Nicolás, A., Flores-Nicolás, M., Menchaca-Campos, E. C., & Uruchurtu-Chavarín, J. (2025a). Mechanical Behavior of Concrete Reinforced with Natural Palm and Mango Fibers. Journal of Engineering and Technological Sciences, 57(1), 48–65. https://doi.org/10.5614/j.eng.technol.sci.2025.57.1.4.

Flores-Nicolás, A., Flores-Nicolás, M., Menchaca-Campos, E. C., & Uruchurtu-Chavarín, J. (2025b). STUDY ON CORROSION OF REINFORCED CONCRETE WITH SYNTHETIC FIBER USING ELECTROCHEMICAL NOISE TECHNIQUE. Civil and Environmental Engineering, 28(1), 271–281. https://doi.org/10.2478/cee-2025-0021.

Hemeda, E. S., Bashandy, A. A., & Nasser, A. A. (2024). IMPROVING MECHANICAL PROPERTIES OF RECYCLED AGGREGATE PERVIOUS CONCRETE USING TAGUCHI METHOD. Civil and Environmental Engineering, 20(2), 1186–1202. https://doi.org/10.2478/cee-2024-0087.

Hoang, D. P., Pham, D. T., Cao, M. Q., & Tran, M. T. (2025). EFFECT OF SHORT POLYPROPYLENE FIBRE CONTENT ON THE MECHANICAL PROPERTIES OF TEXTILE-REINFORCED ENGINEERED CONCRETE COMPOSITE. Civil and Environmental Engineering, 28(1), 521–534. https://doi.org/10.2478/cee-2025-0039.

Iqbal, S., Ali, I., Room, S., Khan, S. A., & Ali, A. (2019a). Enhanced mechanical properties of fiber reinforced concrete using closed steel fibers. Materials and Structures/Materiaux et Constructions, 52(3). https://doi.org/10.1617/s11527-019-1357-6.

Iqbal, S., Ali, I., Room, S., Khan, S. A., & Ali, A. (2019b). Enhanced mechanical properties of fiber reinforced concrete using closed steel fibers. Materials and Structures/Materiaux et Constructions, 52(3). https://doi.org/10.1617/s11527-019-1357-6.

Irmawan, M., Piscesa, B., Alrasyid, H., & Suprobo, P. (2022). Numerical Modeling of Steel Fiber Reinforced Concrete Beam with Notched under Three-point Bending Test. Civil Engineering and Architecture, 10(7), 3227–3242. https://doi.org/10.13189/cea.2022.100733.

Jin, A. H., Woo, J. S., Yun, H. Do, Kim, S. W., Park, W. S., & Choi, W. C. (2025). Influence of concrete strength and fiber properties on residual flexural strength of steel fiber-reinforced concrete. Construction and Building Materials, 489. https://doi.org/10.1016/j.conbuildmat.2025.142366.

Kaklauskas, G., Sokolov, A., & Barros, J. A. O. de. (2024). A design methodology for fibre reinforced concrete elements in serviceability conditions integrating tension softening and stiffening effects. Engineering Structures, 311. https://doi.org/10.1016/j.engstruct.2024.118199.

Khalilpour, S., BaniAsad, E., & Dehestani, M. (2019). A review on concrete fracture energy and effective parameters. In Cement and Concrete Research (Vol. 120, pp. 294–321). Elsevier Ltd. https://doi.org/10.1016/j.cemconres.2019.03.013.

Kim, M. J., Yoo, D. Y., Kim, S., Shin, M., & Banthia, N. (2018). Effects of fiber geometry and cryogenic condition on mechanical properties of ultra-high-performance fiber-reinforced concrete. Cement and Concrete Research, 107, 30–40. https://doi.org/10.1016/j.cemconres.2018.02.003.

Lee, S. J., Yoo, D. Y., & Moon, D. Y. (2019). Effects of hooked-end steel fiber geometry and volume fraction on the flexural behavior of concrete pedestrian decks. Applied Sciences (Switzerland), 9(6). https://doi.org/10.3390/app9061241.

Marcalikova, Z., & Cajka, R. (2020). Determination of Mechanical Properties of Fiber Reinforced Concrete for Numerical Modelling. Civil and Environmental Engineering, 16(1), 86–106. https://doi.org/10.2478/cee-2020-0010.

Meda, A., Minelli, F., & Plizzari, G. A. (2012a). Flexural behaviour of RC beams in fibre reinforced concrete. Composites Part B: Engineering, 43(8), 2930–2937. https://doi.org/10.1016/j.compositesb.2012.06.003.

Meda, A., Minelli, F., & Plizzari, G. A. (2012b). Flexural behaviour of RC beams in fibre reinforced concrete. Composites Part B: Engineering, 43(8), 2930–2937. https://doi.org/10.1016/j.compositesb.2012.06.003.

Mi, Z., Hu, Y., Li, Q., Wang, Y., Zhang, H., & Zhang, Z. (2023). An inverse analysis method for determining tensile softening relationship of concrete considering local response. Construction and Building Materials, 394. https://doi.org/10.1016/j.conbuildmat.2023.132195.

Mishra, A., Chandraul, K., & Kumar Singh, M. (2017). EXPERIMENTAL STUDY ON STEEL FIBER REINFORCED CONCRETE. International Research Journal of Engineering and Technology. www.irjet.net.

Njyman, A. J., & Hilal, A. A. (2025). OPTIMIZING STRENGTH AND IMPACT OF HYBRID FIBER REINFORCED MODIFIED FOAMED CONCRETE BY RESPONSE SURFACE METHOD (RSM). Civil and Environmental Engineering, 28(1), 462–474. https://doi.org/10.2478/cee-2025-0035.

Paegle, I., Minelli, F., & Fischer, G. (2016). Cracking and load-deformation behavior of fiber reinforced concrete: Influence of testing method. Cement and Concrete Composites, 73, 147–163. https://doi.org/10.1016/j.cemconcomp.2016.06.012.

Piscesa, B., Alrasyid, H., Prasetya, D., & Iranata, D. (2021). Numerical Investigation of Reinforced Concrete Beam Due to Shear Failure. IPTEK The Journal for Technology and Science, 31(3), 373. https://doi.org/10.12962/j20882033.v31i3.7385.

Piscesa, B., Attard, M. M., Prasetya, D., & Samani, A. K. (2019). Modeling cover spalling behavior in high strength reinforced concrete columns using a plasticity-fracture model. Engineering Structures, 196. https://doi.org/10.1016/j.engstruct.2019.109336.

Piscesa, B., Attard, M. M., & Samani, A. K. (2018). 3D Finite element modeling of circular reinforced concrete columns confined with FRP using a plasticity based formulation. Composite Structures, 194, 478–493. https://doi.org/10.1016/j.compstruct.2018.04.039.

Piscesa, B., Attard, M. M., Samani, A. K., & Tangaramvong, S. (2017). Plasticity constitutive model for stress-strain relationship of confined concrete. ACI Materials Journal, 114(2), 361–371. https://doi.org/10.14359/51689428.

Puspitasari, N. D., Piscesa, B., Attard, M. M., Prasetya, D., Faimun, F., Aji, P., & Suprobo, P. (n.d.). Parameter Identification for Modeling Steel Fiber Reinforced Concrete under Compression to Prevent Concrete Cover Spalling under Severe Earthquake Loading Condition. https://doi.org/10.1051/e3sconf/20201560.

Rashidi, M., Kargar, S., & Roshani, S. (2024). Experimental and numerical investigation of steel fiber concrete fracture energy. Structures, 59. https://doi.org/10.1016/j.istruc.2023.105792.

Rismayanti, I., Piscesa, B., Komara, I., & Irmawan, M. (2025). Crack Mouth Opening Displacement (CMOD) Measurement Techniques for Fiber Reinforced Concrete: A Comprehensive Review. In E. M. Nia, M. Awang, M. F. N. Aulady, M. Traykova, & L. Yola (Eds.), Selected Articles from the 8th International Conference on Architecture and Civil Engineering (pp. 962–973). Springer Nature Singapore.

Salman, A., Hassan, A., & Ahmed, H. I. (2024). Effects of steel fibers and carbon nanotubes on the flexural behavior of hybrid GFRP/steel reinforced concrete beams. Beni-Suef University Journal of Basic and Applied Sciences, 13(1). https://doi.org/10.1186/s43088-024-00584-9.

Samani, A. K., & Attard, M. M. (2012). A stress-strain model for uniaxial and confined concrete under compression. Engineering Structures, 41, 335–349. https://doi.org/10.1016/j.engstruct.2012.03.027.

Tariq, K. A., Ahmad, J., Husnain, S. A., & Ijaz, M. S. (2023). Influence on compressive and tensile strength properties of fiber-reinforced concrete using polypropylene, jute, and coir fiber. Journal of the Mechanical Behavior of Materials, 32(1). https://doi.org/10.1515/jmbm-2022-0263.

Velayutham, G., & Cheah, C. B. (n.d.). The Effects of Steel Fibre on the Mechanical Strength and Durability of Steel Fibre Reinforced High Strength Concrete (SFRHSC) Subjected to Normal and Hygrothermal Curing. https://doi.org/10.1051/C.

Wang, X., Xu, B., Mu, R., Qing, L., Liu, Y., Chen, X., Chen, J., & Lei, Z. (2023). Flexural properties of a 2D-distributed steel fiber reinforced cement-based composite two-way slab. Journal of Building Engineering, 73. https://doi.org/10.1016/j.jobe.2023.106792.

Yoo, D. Y., & Yoon, Y. S. (2015). Structural performance of ultra-high-performance concrete beams with different steel fibers. Engineering Structures, 102, 409–423. https://doi.org/10.1016/j.engstruct.2015.08.029.

Zhang, J., & Stang, H. (1998). APPLICATIONS OF STRESS CRACK WIDTH RELATIONSHIP IN PREDICTING THE FLEXURAL BEHAVIOR OF FIBRE-REINFORCED CONCRETE.

Zhang, P., Wang, C., Gao, Z., & Wang, F. (2023). A review on fracture properties of steel fiber reinforced concrete. In Journal of Building Engineering (Vol. 67). Elsevier Ltd. https://doi.org/10.1016/j.jobe.2023.105975.

Zhang, Y., Ju, J. W., Chen, Q., Yan, Z., Zhu, H., & Jiang, Z. (2020). Characterizing and analyzing the residual interfacial behavior of steel fibers embedded into cement-based matrices after exposure to high temperatures. Composites Part B: Engineering, 191. https://doi.org/10.1016/j.compositesb.2020.107933.

Zhao, Y., Wu, B., Peng, S., Yu, Z., & Du, X. (2023). Research and mechanism analysis on dynamic compressive behavior of steel fiber reinforced concrete. Construction and Building Materials, 368. https://doi.org/10.1016/j.conbuildmat.2023.130358.

How to Cite This Article

Setiamanah, D. T., Suprobo, P., Piscesa, B., Salma, S. N., Ramzy, A. K., Sukmajaya, P. P., Aspar, W. A. N., Purnomo, D. A., Agustin, W., & Lathif, S. (2026). Experimental and Numerical Investigation of Flexural Behaviour in Steel Fiber-Reinforced Concrete Notched Beam. Civil and Environmental Engineering, 0 (0). https://doi.org/10.2478/cee-2026-0082